inorganics

MDPI

Article

Antibacterial Activity of Oxygen Vacancy-Mediated ROS Production of V_6O_{13} Powder against *Candida albicans*

Li Liu [1,2], Siyu Li [3], Detai Shi [1], Qifu Bao [1], Tiangui Zhao [1], Wei Zhu [2], Xiaolong Li [1] and Jianer Zhou [1,*]

[1] School of Materials Science and Engineering, Jingdezhen Ceramic University, Jingdezhen 333403, China; llmb20@hotmail.com (L.L.); 001230@jcu.edu.cn (D.S.); dwxbqf0727@163.com (Q.B.); tgzhao524@163.com (T.Z.); m18270985763@163.com (X.L.)
[2] Department of Mathematics and Physics, Quzhou University, Quzhou 324000, China; 13867024969@163.com
[3] National Engineering Research Center for Cereal Fermentation and Food Biomanufacturing, Jiangnan University, Wuxi 214000, China; li3642103@163.com
* Correspondence: msejdz@hotmail.com

Abstract: The emergence of drug resistance due to the overuse of antibiotics has made the prevention and treatment of invasive fungal infections caused by *Candida albicans* (*C. albicans*) a great challenge. Oxygen vacancy-rich inorganic materials show great promise in the antimicrobial field due to their unique physicochemical properties. Defect engineering can significantly optimize the electronic structure of inorganic materials to further enhance their antimicrobial activity. We designed oxygen vacancy defect-rich V_6O_{13} powders using the hydrothermal-calcination method and investigated their anti-*C. albicans* activity. The results showed that the stronger antibacterial activity is attributed to the fact that the optimized V_6O_{13} powder oxygen vacancy defects induced a reduction reaction of dissolved oxygen in the environment, which produced ROS with strong oxidative properties, causing damage to the wall membrane of *C. albicans* and leakage of intracellular material. The minimum inhibitory concentration (99% or more inhibition) of V_6O_{13} powders is 4 mg/mL. This work not only provides a facile method for constructing oxygen-rich vacancies in V_6O_{13} powders, but also provides new insights into the potential of inorganic materials optimized by defect engineering for efficient antimicrobial activity.

Keywords: *C. albicans*; V_6O_{13}; oxygen vacancy; antibacterial properties

Citation: Liu, L.; Li, S.; Shi, D.; Bao, Q.; Zhao, T.; Zhu, W.; Li, X.; Zhou, J. Antibacterial Activity of Oxygen Vacancy-Mediated ROS Production of V_6O_{13} Powder against *Candida albicans*. *Inorganics* **2023**, *11*, 429. https://doi.org/10.3390/inorganics11110429

Academic Editor: Guido Kickelbick

Received: 9 September 2023
Revised: 18 October 2023
Accepted: 29 October 2023
Published: 2 November 2023

1. Introduction

Globally, more than 1 billion people suffer from fungal infections each year, resulting in 1.6 million deaths [1–3]. *C. albicans* accounts for 40% of the total mortality from all fungal infections [4]. *C. albicans* infections are commonly treated with azoles, polyenes, and echinocandins [5]. However, these antifungal drugs have limitations in terms of toxicity, recurrence of infection, and the emergence of drug resistance [6]. The application of inorganic antibacterial materials is one of the ways to solve this problem [7–10].

In recent years, antibacterial inorganic antimicrobial materials have become a hot research topic [11,12]. Compared with metal ion (Ag, Cu, Zn, etc.) and photocatalytic (TiO_2, ZnO, SnO_2, etc.) inorganic antimicrobial materials, metal oxide (ZnO, CuO, CaO, MgO, vanadium oxide, etc.) antimicrobial materials have the most important advantage of combining the characteristics of the above two types of antimicrobial materials [10,11,13,14]. This type of inorganic antimicrobial material has a wider range of uses and low cost, and the metal ions produced in the process of antimicrobial sterilization are the elements needed for human growth, which makes them more biocompatible.

Recently, the bactericidal properties of vanadium oxides have attracted attention [15–17]. Vanadium has a variety of oxidation states and coordination environments that affect color, semiconductor to metal phase transitions, and oxide phase formation, with V_2O_3, V_2O_5, V_6O_{13}, and VO_2 being some of the most common oxide phases [18–20]. Oxygen

vacancy defects, a common type of point defects, are widely present in vanadium oxides and affect the local geometries and electronic structures of the materials, generating unsaturated coordination sites that lead to the formation of a large number of active sites. Researchers have utilized different approaches to create oxygen vacancy defects in vanadium oxides [21–23]; for example, by building specific structures and particle sizes and changing the phase transition temperature to achieve excellent antibacterial effects [24–27]. Oxygen vacancy defects are also an important factor in the oxidative damage mechanism of ROS [28–30], and inorganic materials with oxygen vacancy defects show unique advantages in terms of antimicrobial activity. The mechanism of the antimicrobial activity of vanadium oxides is mainly attributed to the oxidative stress of reactive oxygen species (ROS) leading to cell death. Researchers have utilized different methods to create oxygen vacancy defects in vanadium oxides. For example, vanadium oxides with abundant oxygen vacancy defects have been prepared by means of elemental doping [31], water vapor activation [32], the electron beam evaporation method [33], exposure to plasma [34], etc. Therefore, V_6O_{13} powders rich in oxygen vacancy defects are worth exploring in depth in terms of anti-*Candida albicans*.

In this study, a series of V_6O_{13} powders was prepared by hydrothermal reaction and calcination in argon atmosphere using ammonium metavanadate and anhydrous oxalic acid as raw materials. The materials were characterized by XRD, SEM, TEM, and XPS, and then, the antibacterial effect of V_6O_{13} powders against *C. albicans* was investigated. The minimum inhibitory concentration of V_6O_{13} powders is 4 mg/mL. Finally, it is proposed that the oxygen vacancy defect of V_6O_{13} powder can trap oxygen molecules and enhance the activity of V_6O_{13} powder, which in turn promotes the production of intracellular ROS, disrupts the morphology and membrane integrity of *C. albicans*, and achieves antibacterial activity. This work investigates the production of oxygen vacancies in V_6O_{13} powders and understands the role of oxygen vacancy defects in ROS production and the resulting antimicrobial activity. This has important implications for the design of more effective vanadium oxide based antimicrobial materials.

2. Experiment

2.1. Materials and Synthesis

Ammonium metavanadate (NH_4VO_3) and anhydrous oxalic acid ($C_2H_2O_4$) were purchased from Aladdin Co. Ltd. (Shanghai, China), and all chemicals were analytically pure and not purified. NH_4VO_3 and $C_2H_2O_4$ were added to 80 mL of deionized water in a molar ratio of 2:3 and stirred for 1 h at room temperature to obtain a blue liquid. Then, the balance solution was transferred into a 100 mL Teflon autoclave and kept in an oven at 180 °C for 0.5 h, 3 h, 6 h, 9 h, 12 h reaction times, respectively. After cooling for room temperature, the black product was washed several times with deionized water and ethyl alcohol. After drying in a vacuum at 65 °C for 12 h, the final products were successfully obtained by calcining at 650 °C for 2 h in high purity argon. For simplicity, the samples were labelled S1, S2, S3, S4, and S5 in order of hydrothermal reaction times of 0.5 h, 3 h, 6 h, 9 h, and 12 h after calcination in argon atmosphere.

2.2. Materials Characterization

The crystal structures of the synthesized samples were analyzed using a Bruker D8 Advance powder X-ray diffractometer (XRD, Bruker AXS D8-Advance, Berlin, Germany) and a Cu Kα source. Surface morphology was observed uisng a field emission scanning electron microscope (FE-SEM, HITACHI SU8010, Tokyo, Japan). Transmission electron microscopy (TEM, JEOL JEM-2010(HR), Tokyo, Japan) images were operated at an accelerating voltage of 200 kV, equipped with selected area electron diffraction (SAED) and high-resolution transmission electron microscopy (HRTEM). X-ray photoelectron spectra (XPS, Thermo-Fischer, ESCALAB Xi+, New York, NY, USA) were measured with Al Kα radiation.

2.3. Antibacterial Experiments

2.3.1. Strains, Media and Conditions

In this study, *C. albicans* ATCC^{10231} was used to evaluate the potential antimicrobial effect of V_6O_{13}. V_6O_{13} powder, Sabouraud Dextrose Medium (SDM), and deionized water were autoclaved, 121 °C, for 20 min. SDM medium consists of 40 g glucose, 10 g peptone and deionized water to 1 L. The solid medium was supplemented with 20 g of agar. *C. albicans* ATCC^{10231} seed was added to a 24-well plate containing 5 mL of SDM medium to a final concentration of approximately 1×10^5 cells/mL, and V_6O_{13} powder was added to the desired final concentration. Then, 24-well plates were fixed on a shaker and incubated at a constant temperature of 30 °C with shaking at 200 r/min. Samples were taken at certain times for relevant assays.

2.3.2. Antibacterial Circle Test

The inhibitory activity of samples S1, S2, S3, S4, and S5 was determined by measuring the size of the diameter of the inhibition circle. Several small wells were punched on plates coated with SDM of *C. albicans* ATCC^{10231}, and 30 μL of a mixture of powder at a final concentration of 100 mg/mL and deionized water was added to the wells. The plates were incubated at 30 °C for 24 h. The diameter of the zone of inhibition was measured, and the test was repeated three times independently under the same experimental conditions, with the final results expressed as mean ± standard deviation.

2.3.3. Antibacterial Rate Test

S1, S2, S3, S4, and S5 powders were co-cultured by adding SDM medium containing 1×10^5 cells/mL of bacteria in 24-well plates, respectively, with a final concentration of 2.5 mg/mL of powder. The culture conditions were as described previously. At 24 h, 50 μL of sample solution was taken, diluted to the appropriate concentration, and then 100 μL was taken and applied uniformly to the surface of the plates covered with SDM. The plates were incubated at 30 °C for 24 h. The number of bacteria in the diluted solution was calculated by counting the number of colonies, and was then converted to the number of bacteria in the original solution. Bacterial inhibition rate was defined as:

$$R\ (\%) = (A - B)/A * 100\%, \quad (1)$$

where R is the percentage reduction of *C. albicans* ATCC^{10231}, A is the average number of viable bacteria in the control group, and B is the average number of viable bacteria in the samples. Each group of experiments was repeated three times.

2.3.4. Minimum Inhibition Concentration Test

The minimum inhibitory concentration was determined by co-incubating S3 samples with bacteria for 24 h. The final concentrations of S3 samples were: 1.5, 2, 3, and 4 mg/mL, and 4 mg/mL of non-inhibitory powder was added to the control group. The inhibition rate was determined in the same way as before. Three replicates were performed for each group of experiments.

2.3.5. Reactive Oxygen Testing

S3 powder was co-cultured with *C. albicans* in SDM liquid medium at a final concentration of 3 mg/mL. No powder was added to control 1 and a powder without antimicrobial effect was added to control 2. Then, 1 mL fermentation broth was taken at 0.5 h, 2 h, and 12 h, and centrifuged at 6000 rmp for 10 min. The supernatant was discarded. The organisms were collected and washed twice with PBS, and then diluted to the appropriate concentration. After collecting the co-cultured organisms in PBS, DCFH-DA fluorescent probe (S0060, Beyotime, Shanghai, China), at a concentration of 10 μM, was added and a metal bath was used for 30 min at 37 °C. To remove the DCFH-DA that did not enter the cells, the cells were washed three times with sterilized PBS. Fluorescence detection

was performed by adding 200 μL of sample solution to a 96-well plate, which was placed into a multifunctional zymograph, using a Tecan-spark plate reader (Tecan, Männedorf, Switzerland) with an absorption wavelength of 488 nm, an emission wavelength of 535 nm, and a gain value of 100. To detect the amount of cell growth, 200 μL of sample solution was added to a 96-well clear plate and the absorption wavelength was set to 600. ROS value = fluorescence intensity/OD600. Three replicates of each set of experiments were performed.

2.3.6. Protein Leak Detection

The concentration of extracellular proteins was detected using the KOMAS Brilliant Blue method. Bovine serum protein was prepared to final concentrations of 0, 0.02, 0.04, 0.06, 0.08, and 0.10 mg/mL and reacted with KOMAS Brilliant Blue to obtain a standard curve of protein concentration versus absorbance at 595 nm, Y = 0.3138*X − 0.0029. Then, 1 mL of fermentation broth was taken at 0.5 h, 2 h, and 12 h and was centrifuged at 6000 rmp. After centrifugation for 10 min, 50 μL of supernatant and 150 μL of KOMAS Brilliant Blue were added to 96-well plates for absorbance detection. The absorbance value of the protein was obtained by subtracting the absorbance of KOMAS Brilliant Blue control solution from the obtained value, and then the total protein content was derived from the standard curve. Three replicates of each set of experiments were performed.

2.3.7. Bacterial Morphology Scan

Changes in the morphology and internal structure of the organisms were observed by scanning electron microscopy (SEM, HITACHI SU8100, Tokyo, Japan) and transmission electron microscopy (TEM, HITACHI HT7800, Tokyo, Japan). A final concentration of 2 mg/mL of S3 powder was co-cultured with *C. albicans* for 24 h. No powder was added to control 1 and a powder without antimicrobial effect was added to control 2. Cultured specimens were fixed in a cold solution of 2.5% glutaraldehyde for 4 h and were then rinsed three times with deionized water. Next, the samples were dehydrated and naturally dried with gradients of ethanol (30%, 50%, 70%, 80%, 90%, and 100%). The SEM method was performed by drying, gold spraying, and scanning electron microscopy on the samples. The TEM method was performed under overnight treatment with embedding agent; the permeable samples were embedded and heated overnight at 70 °C to obtain the embedded samples. Samples were sectioned with an ultrathin sectioning machine, stained with lead citrate solution and 50% ethanol saturated uranium acetate solution for 5–10 min each, and observed with a transmission electron microscope.

3. Results and Discussion

3.1. Characterizations of Materials

Figure 1 shows the XRD analysis profiles of samples S1, S2, S3, S4, and S5. The sample S1 showed pure V_6O_{13} (JCPDS file No. 43-1050, space group: C2/m) phase at hydrothermal time of 0.5 h. With the increase of reaction time, samples S2, S3, S4, and S5 started to show VO_2 (JCPDS file No. 43-1051, space group: P21/c) phase, and the intensity of the peak increased with time. The variation of V_6O_{13} with hydrothermal time can be described as follows: $V_6O_{13} \rightarrow V_6O_{13}$ + part of VO_2. These results are consistent with previous reports [35]. For the phase transition in V_6O_{13}, it has been reported that the synergistic motion of VO_6 octahedra in V_6O_{13} plays an important role, where some oxygen is released during the formation of VO_2 and transferred to the surface by diffusion, and the free energy of the system is subsequently reduced [36].

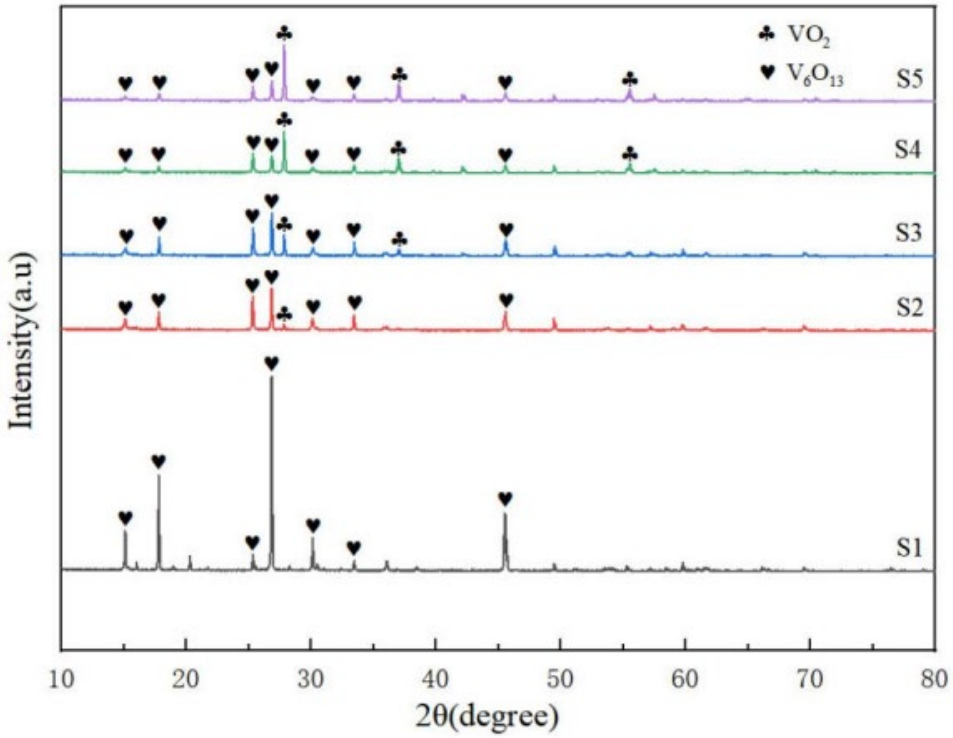

Figure 1. XRD pattern of the samples obtained at 180 °C for: (S1) 0.5 h, (S2) 3 h, (S3) 6 h, (S4) 9 h, (S5) 12 h.

Figure 2 shows the SEM images of S1, S2, S3, S4, and S5 samples. When the reaction time is 0.5 h and 3 h, the columnar shape of the samples is observed. When the reaction time is 6 h, some small particles and columnar aggregates are obtained. As the reaction time increased to 9 h and 12 h, the granularity in the samples gradually increased and the columnar shape became less.

Figure 3 shows the TEM images of the synthesized sample S3 after a hydrothermal time of 6 h and calcination by argon gas. As shown in Figure 3a,b, the synthesized V_6O_{13} has a columnar morphology. Figure 3c shows the selected area electron diffraction (SAED) pattern phase of sample S3. The SAED pattern of the sample is indexed as V_6O_{13}, which also indicates that V_6O_{13} is single-crystalline. Figure 3d shows the high-resolution transmission electron microscopy (HRTEM) image of sample S3. The lattice edges of V_6O_{13} show d-spacings of 5.84 Å and 3.5 Å, which correspond to the interplanar spacing of the (200) and (110) faces of V_6O_{13}, respectively [37–39]. These results are also in good agreement with the XRD results.

The type and presence state of the elements on the surface of the material were characterized by XPS. V, O, and C are recorded in the measured spectra as shown in Figure 4a, indicating high purity without other impurities. The high-resolution V2p spectra of the S3 sample (Figure 4b) indicate the presence of V ions in two different oxidation states, with peaks at binding energies of 523.24 eV and 516.15 eV corresponding to V^{4+} and peaks at binding energies of 524.56 eV and 517.54 eV corresponding to V^{5+}, a result that is in good agreement with the chemical state of vanadium in V_6O_{13} reported in the literature [31,40,41]. O1s high resolution spectrum (Figure 4b) shows the presence of vacant oxygen in sample S3, with peaks at binding energies of 529.82 eV corresponding to lattice oxygen (O_{latt}) and 530.69 eV corresponding to vacant oxygen (O_d) [34]. The high resolution spectra of S1, S2, S3, S4, and S5 V2p spectra (Figure 4c) and O1s spectra (Figure 4d) indicate the presence of V^{4+} and V^{5+} as well as oxygen vacancies at similar and variable levels in all samples.

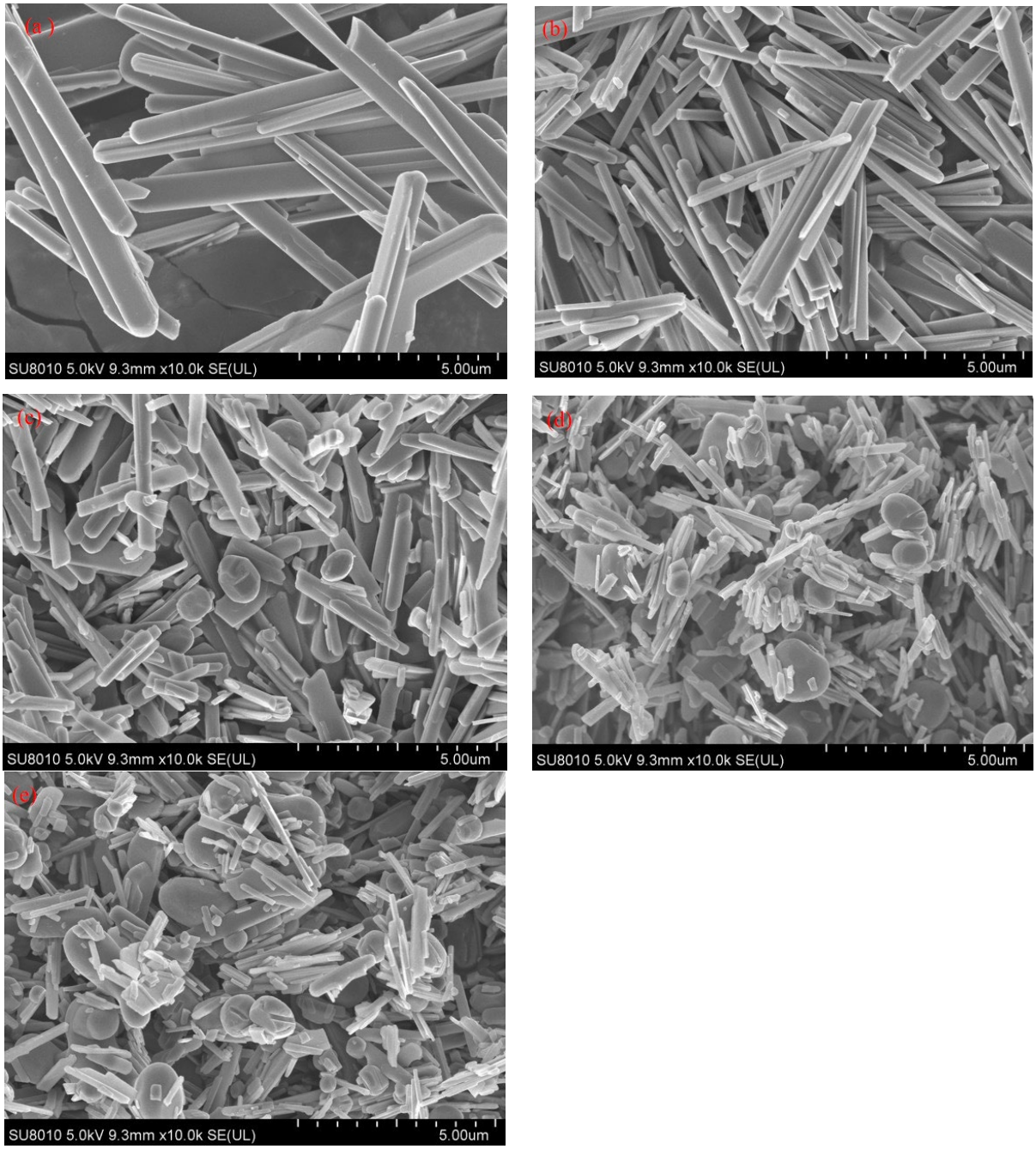

Figure 2. SEM images of the synthesized samples: (**a**) S1, (**b**) S2, (**c**) S3, (**d**) S4, (**e**) S5.

Fourier transform infrared spectroscopy (FT-IR) is a rotational vibrational spectroscopy technique, which is based on the absorption of photons by the molecules of a material [42]. Figure 5 shows the results of the FT-IR spectra of S1–S5, where the signals between 500 and 1000 cm^{-1} can be attributed to various vibrations of the V-O bonds [43]. The absorption peaks of S1–S5 appearing at 527 cm^{-1} are attributed to the stretching mode of oxygen shared by three vanadium atoms [44]. The peaks of S2–S5 appearing at 893 cm^{-1} and 1003 cm^{-1} represent the vibrations of the V-O bond, and the structure and composition of the sample can be attributed to VO_2 [45,46].The results of XRD and FT-IR spectroscopic analyses show that VO_2 with a monoclinic phase structure appeared gradually with the increase of the hydrothermal temperature.

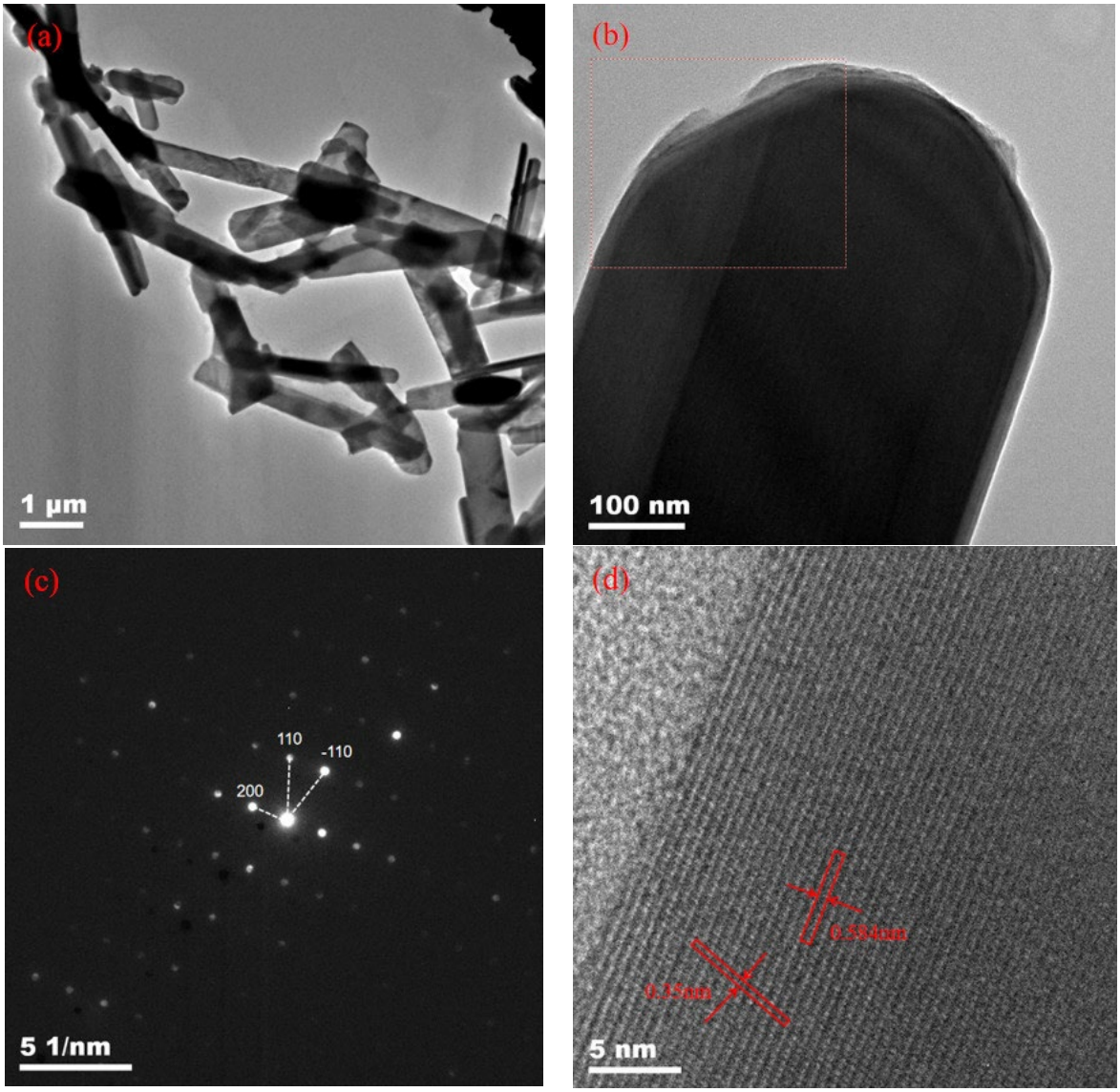

Figure 3. TEM images of S3 sample: (**a**,**b**) TEM images, (**c**) SAED image, (**d**) HRTEM image.

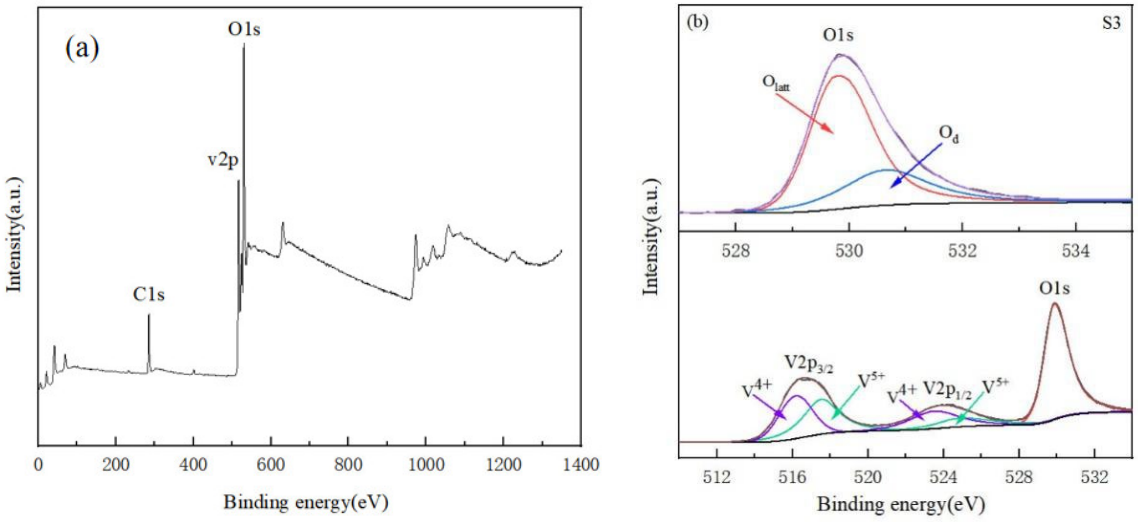

Figure 4. *Cont*.

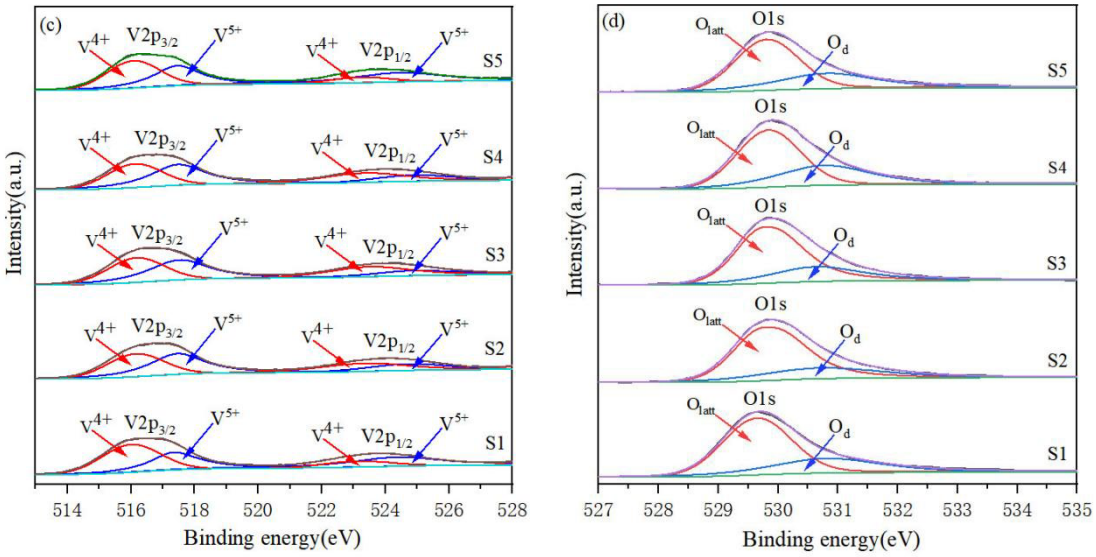

Figure 4. (**a**) The XPS survey spectrum of S3; (**b**) High-resolution V2p spectra and O1s spectra of S3; (**c**) High-resolution V2p spectra of S1, S2, S3, S4, and S5; (**d**) High-resolution O1s spectra of S1, S2, S3, S4, and S5.

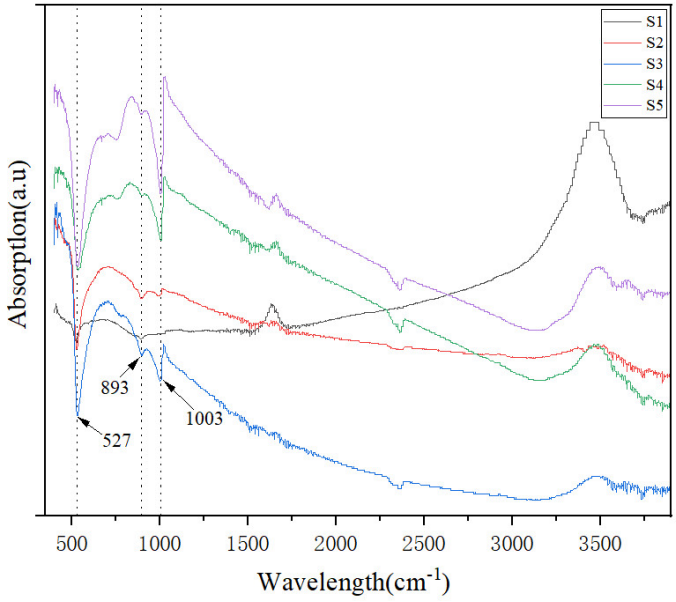

Figure 5. FT-IR spectra of samples S1, S2, S3, S4, and S5.

3.2. Antibacterial Properties

In the present study, we first examined the inhibition of S1, S2, S3, S4, and S5 powders in *C. albicans* with inhibition circle diameters of 0.69 ± 0.08 cm, 0.98 ± 0.04 cm, 1.07 ± 0.04 cm, 0.98 ± 0.01 cm, and 0.63 ± 0.01 cm, respectively, and the inhibition circle diameters became larger and then became smaller (Figure 6). The largest diameter of the inhibition circle is S3, indicating that the sample has the best antibacterial effect.

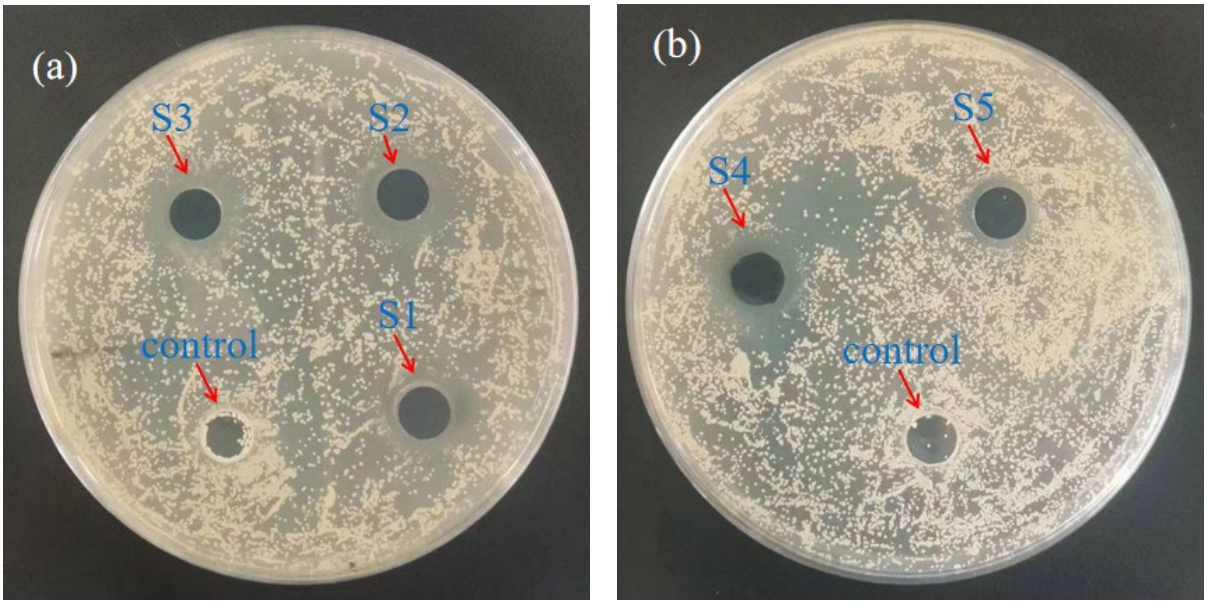

Figure 6. S1, S2, S3, S4, and S5 powders against *C. albicans* after 24 h. (**a**) Zone of the inhibition test for S1, S2, and S3. (**b**) Zone of the inhibition test for S4 and S5. Control represents no powder added.

To further test the ability of the powder to inhibit bacteria, we examined the inhibition rates of S1, S2, S3, S4, and S5. Briefly, *C. albicans* ATCC^{10231} and the powder were co-cultured for 24 h, and the fermentation broth diluted to a certain concentration was taken and applied to the solid medium for 24 h, colonies were counted, and the inhibition rate was calculated. The inhibition rates of S1, S2, S3, S4, and S5 were 74.8 ± 0.12%, 79.9 ± 0.25%, 92.9 ± 0.34%, 92 ± 0.27%, and 58.7 ± 0.22%, respectively (Figure 7). The inhibition was the first to become stronger and then weaker. Among them, S3 has the highest inhibition rate, which means it is the strongest. From the inhibition circle and inhibition rate, S3 has the best inhibition effect, so we chose the S3 sample for the following experiments.

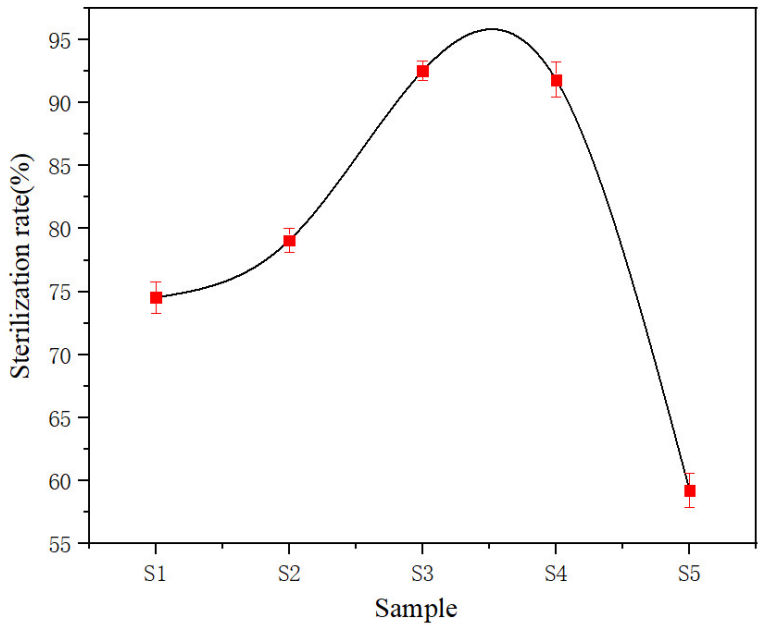

Figure 7. Graph of bacterial inhibition rate of S1, S2, S3, S4, and S5 samples.

The minimum inhibition concentration is an important indicator of the magnitude of antimicrobial activity of antimicrobial materials. We incubated the S3 sample with *C. albicans* for 24 h, took the fermentation broth and diluted it a certain number of times, then coated the plate medium, and counted the number of colonies to calculate the inhibition rate. Minimum inhibitory concentration (MIC) was defined as a 99% or more antibacterial rate. The corresponding inhibition rates for S3 samples with final concentrations of 1.5, 2, 3, and 4 mg/mL were 22.60 ± 0.07%, 65.63 ± 0.05%, 97.22 ± 0.02%, and 99.57 ± 0.03%, respectively, indicating an MIC of 4 mg/mL.

To observe whether the cell phenotype and internal structure were changed, we performed biological SEM and TEM analyses. To obtain the co-presence of intact and damaged cells, we selected S3 samples at a final concentration of 2 mg/mL to be co-cultured with *C. albicans*. SEM results showed that cells of control 1 and control 2 were intact. However, the cells co-cultured with S3 were significantly damaged. The main manifestation was that most of the cells were crumpled. The surface cell wall of uncrumpled cells was detached and it produced raised pockets on its surface, indicating that the cell membrane was attacked and the mechanical properties deteriorated, while the intracellular material was disturbed and leaked outward (Figure 8a). The TEM results showed that, compared with the control, the co-culture of cells and S3 powder resulted in cell crumpling, irregular mass wall separation, and the condensation of intracellular material into small black dots (Figure 8b).

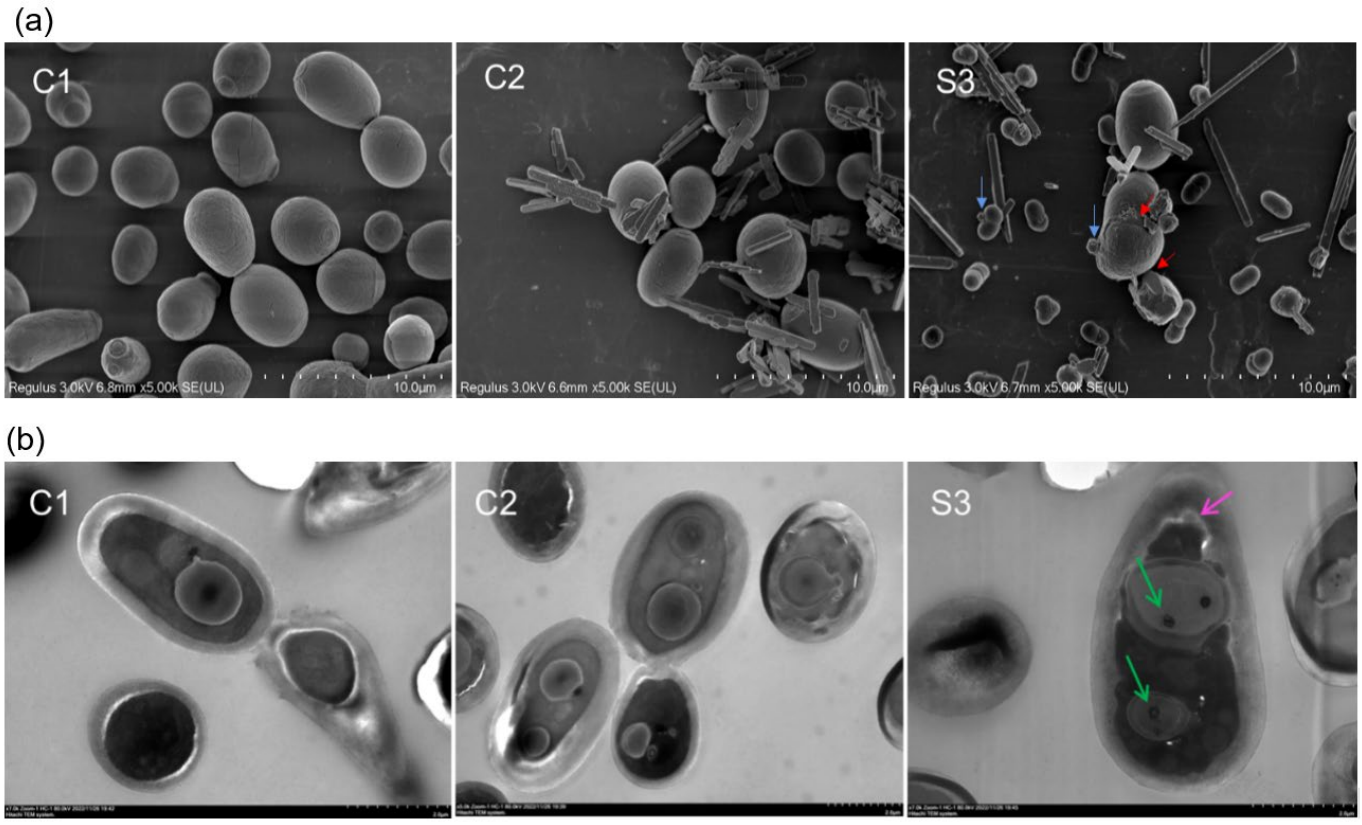

Figure 8. SEM and TEM analyses of *C. albicans* after co-culture with S3. (**a**) SEM image of *C. albicans* after co-culture with S3, (**b**) TEM image of *C. albicans* after co-culture with S3. C1 represents no powder, C2 represents co-culture with powder without antimicrobial effect, and S3 represents co-culture with S3 at a final concentration of 2 mg/mL. Blue-arrows indicate leaking sachets. Red-arrows indicate damaged cell envelope. Green-arrows indicate concentrated contents of organelles. Pink arrow indicates plasma wall separation.

Cellular damage is often due to excessive elevation of reactive oxygen species, and the production of excess ROS disrupts bacterial membranes and genetic material, thereby inhibiting the growth and reproduction of *C. albicans*. Therefore, we investigated the level of intracellular reactive oxygen species in *C. albicans* after co-culture with S3. The results showed that, after 2 h of co-culture, the ROS of cells in the experimental group with S3 added was more than twice that of the control group, and decreased slightly after 12 h, indicating that the effect of S3 on cellular ROS was mainly in the early stage of co-culture (Figure 9a). To demonstrate whether the intracellular material was leaked, we examined the protein concentration of the fermentation broth at 0.5 h, 2 h, and 12 h. The results showed that the protein concentration of the fermentation broth co-cultured with S3 was approximately two, four, and eight times higher than that of the control at the corresponding times, indicating that there was a large amount of intracellular protein leakage with increasing co-culture time, which caused cellular crumpling (Figure 9b).

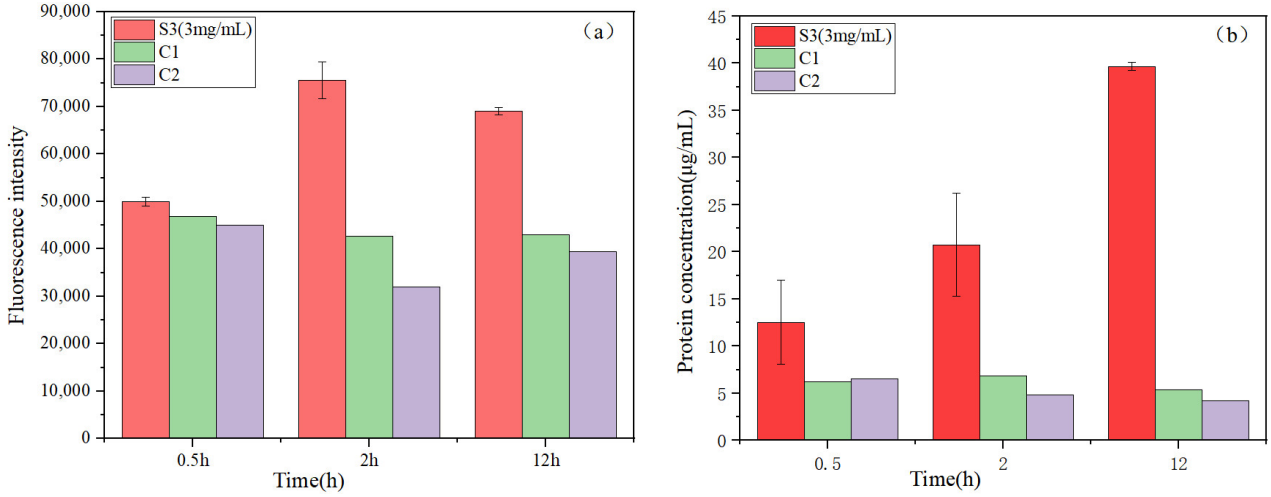

Figure 9. Co-culture of *C. albicans* with S3 powder for reactive oxygen levels and protein leakage. (**a**) Reactive oxygen levels of *C. albicans*. (**b**) Protein concentration of co-culture fermentation broth. The experimental group was spiked with S3 samples at a final concentration of 3 mg/mL. C1 represents the addition of no powder, C2 represents the addition of non-antibacterial powder.

4. Conclusions

In this study, a series of V_6O_{13} materials was prepared using hydrothermal calcination method. By changing the process parameters, the crystallinity and oxygen vacancies of V_6O_{13} were regulated and a conformational relationship was established with its anti-*C. albicans* property, which provided a new way to design and synthesize efficient V_6O_{13} antibacterial materials. It can be seen from the above analysis that V_6O_{13} is subjected to specific external environments (e.g., high temperature, reduction treatment, etc.) resulting in the transformation of crystallinity and the decrease of vanadium ion valence (gradual transition from V^{5+} to V^{4+}), during which the detachment of oxygen from the crystal lattice leads to the formation of oxygen vacancy defects due to oxygen deletion. The defect equation can be expressed as $O = ½O_2 + V_o$. We analyzed the morphology of *C. albicans* after V_6O_{13} treatment in depth by Bio SEM and TEM (Figure 8), and found that the cells were crumpled and became smaller, and intracellular materials were leaked. It was further shown by the results of ROS and protein leakage detection (Figure 9) that the production of excessive ROS destroyed the bacterial membrane, leading to the leakage of genetic material, thus inhibiting the growth and reproduction of *C. albicans*. Samples S1, S2, S3, S4, and S5 all showed better bacterial inhibition, with S3 and S4 reaching 92.9% and 92%, respectively, suggesting that, at a hydrothermal temperature of 180 °C and hydrothermal time of 6–9 h, S3 and S4 reached 92.9% and 92.9%, respectively, indicating that more oxygen vacancy

defects were formed at a hydrothermal temperature of 180 °C and a hydrothermal time of 6–9 h. The samples were calcined at 650 °C for 2 h under an argon environment.

Accordingly, the oxygen vacancy defects formed in the V_6O_{13} powders prepared in the hydrothermal-calcined environment induced a reduction reaction with dissolved oxygen to produce ROS with strong oxidizing properties, and this active substance oxidatively damaged *C. albicans*. Based on the above findings, it can be inferred that the mechanism of the anti-*C. albicans* action of the V_6O_{13} powders in this paper is as shown in Figure 10 To the best of our knowledge, this study identifies for the first time that V_6O_{13} has anti-*C. albicans* ability, and the preparation process is simple and does not introduce foreign substances, which can help with the design of new and potential oxidized-based antimicrobial agents.

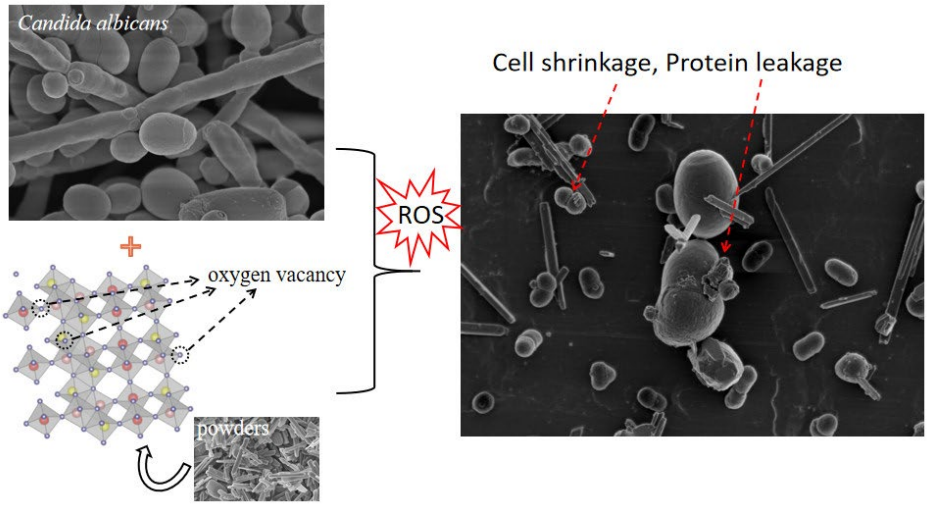

Figure 10. Diagram of the mechanism of the antimicrobial action of V_6O_{13}.

Author Contributions: Conceptualization, L.L., Q.B. and J.Z.; Methodology, L.L. and W.Z.; Software, T.Z. and W.Z.; Validation, S.L. and T.Z.; Formal analysis, W.Z.; Investigation, S.L.; Resources, S.L. and D.S.; Data curation, X.L.; Writing-original draft, L.L.; Writing-review & editing, L.L.; Visualization, Q.B.; Supervision, D.S. and J.Z.; Project administration, X.L. and J.Z.; Funding acqui-sition, D.S. All authors have read and agreed to the published version of the manuscript.

Funding: This thesis was supported by the National Natural Science Foundation of China (22108077), the Natural Science Foundation of Jiangxi Province (20161BAB213067), and the Scientific Research Fund of Jiangxi Provincial Department of Education (GJJ170807). Other than that, there is no other funding. Thank you.

Data Availability Statement: Not applicable.

Acknowledgments: The authors gratefully acknowledge the financial support provided by National Natural Science Foundation of China (Nos. 22108077), the Project Supported by Natural Science Foundation of Jiangxi(20161BAB213067), Scientific Research Fund of Jiangxi Provincial Education Department (GJJ170807).

Conflicts of Interest: The authors declare no conflict of interest.

References

1. Tufa, T.B.; Denning, D.W. The Burden of Fungal Infections in Ethiopia. *J. Fungi* **2019**, *5*, 109. [CrossRef] [PubMed]
2. Wu, Y.; Hu, S.; Wu, C.; Gu, F.; Yang, Y. Probiotics: Potential Novel Therapeutics Against Fungal Infections. *Front. Cell. Infect. Microbiol.* **2021**, *11*, 793419. [CrossRef] [PubMed]
3. Rokas, A. Evolution of the human pathogenic lifestyle in fungi. *Nat. Microbiol.* **2022**, *7*, 607–619. [CrossRef] [PubMed]
4. Huang, T.; Li, X.; Maier, M.; O'Brien-Simpson, N.M.; Heath, D.E.; O'Connor, A.J. Using inorganic nanoparticles to fight fungal infections in the antimicrobial resistant era. *Acta Biomater.* **2023**, *158*, 56–79. [CrossRef] [PubMed]
5. Carmo, P.; Garcia, M.T.; Figueiredo-Godoi, L.M.A.; Lage, A.C.P.; Silva, N.S.D.; Junqueira, J.C. Metal Nanoparticles to Combat *Candida albicans* Infections: An Update. *Microorganisms* **2023**, *11*, 138. [CrossRef] [PubMed]

6. Kaur, J.; Nobile, C.J. Antifungal drug-resistance mechanisms in *Candida* biofilms. *Curr. Opin. Microbiol.* **2023**, *71*, 102237. [CrossRef] [PubMed]
7. Vallet-Regi, M.; Gonzalez, B.; Izquierdo-Barba, I. Nanomaterials as Promising Alternative in the Infection Treatment. *Int. J. Mol. Sci.* **2019**, *20*, 3806. [CrossRef] [PubMed]
8. Wang, B.; Xu, Y.; Shao, D.; Li, L.; Ma, Y.; Li, Y.; Zhu, J.; Shi, X.; Li, W. Inorganic nanomaterials for intelligent photothermal antibacterial applications. *Front. Bioeng. Biotechnol.* **2022**, *10*, 1047598. [CrossRef]
9. Almotairy, A.R.Z.; Amer, A.M.; El-Kady, H.; Elwakil, B.H.; El-Khatib, M.; Eldrieny, A.M. Nanostructured γ-Al_2O_3 Synthesis Using an Arc Discharge Method and its Application as an Antibacterial Agent against XDR Bacteria. *Inorganics* **2023**, *11*, 42. [CrossRef]
10. Mehrabi, M.R.; Soltani, M.; Chiani, M.; Raahemifar, K.; Farhangi, A. Nanomedicine: New Frontiers in Fighting Microbial Infections. *Nanomaterials* **2023**, *13*, 483. [CrossRef]
11. Tsikourkitoudi, V.; Henriques-Normark, B.; Sotiriou, G.A. Inorganic nanoparticle engineering against bacterial infections. *Curr. Opin. Chem. Eng.* **2022**, *38*, 100872. [CrossRef]
12. Ghazzy, A.; Naik, R.R.; Shakya, A.K. Metal–Polymer Nanocomposites: A Promising Approach to Antibacterial Materials. *Polymers* **2023**, *15*, 2167. [CrossRef] [PubMed]
13. Pallavicini, P.; Dacarro, G.; Taglietti, A. Self-Assembled Monolayers of Silver Nanoparticles: From Intrinsic to Switchable Inorganic Antibacterial Surfaces. *Eur. J. Inorg. Chem.* **2018**, *2018*, 4846–4855. [CrossRef]
14. Díaz-Puertas, R.; Álvarez-Martínez, F.J.; Falco, A.; Barrajón-Catalán, E.; Mallavia, R. Phytochemical-Based Nanomaterials against Antibiotic-Resistant Bacteria: An Updated Review. *Polymers* **2023**, *15*, 1392. [CrossRef] [PubMed]
15. Tousley, M.E.; Wren, A.W.; Towler, M.R.; Mellott, N.P. Processing, characterization, and bactericidal activity of undoped and silver-doped vanadium oxides. *Mater. Chem. Phys.* **2012**, *137*, 596–603. [CrossRef]
16. Huang, L.; Yu, L.; Yin, X.; Lin, Y.; Xu, Y.; Niu, Y. Silver nanoparticles with vanadium oxide nanowires loaded into electrospun dressings for efficient healing of bacterium-infected wounds. *J. Colloid Interface Sci.* **2022**, *622*, 117–125. [CrossRef] [PubMed]
17. Guo, J.; Zhou, H.; Wang, J.; Liu, W.; Cheng, M.; Peng, X.; Qin, H.; Wei, J.; Jin, P.; Li, J.; et al. Nano vanadium dioxide films deposited on biomedical titanium: A novel approach for simultaneously enhanced osteogenic and antibacterial effects. *Artif. Cells Nanomed. Biotechnol.* **2018**, *46*, 58–74. [CrossRef]
18. Liu, M.; Su, B.; Tang, Y.; Jiang, X.; Yu, A. Recent Advances in Nanostructured Vanadium Oxides and Composites for Energy Conversion. *Adv. Energy Mater.* **2017**, *7*, 1700885. [CrossRef]
19. Hu, P.; Hu, P.; Vu, T.D.; Li, M.; Wang, S.; Ke, Y.; Zeng, X.; Mai, L.; Long, Y. Vanadium Oxide: Phase Diagrams, Structures, Synthesis, and Applications. *Chem. Rev.* **2023**, *123*, 4353–4415. [CrossRef]
20. Shvets, P.; Dikaya, O.; Maksimova, K.; Goikhman, A. A review of Raman spectroscopy of vanadium oxides. *J. Raman Spectrosc.* **2019**, *50*, 1226–1244. [CrossRef]
21. Sviridova, T.V.; Sadovska, L.Y.; Konstantinova, E.A.; Belyasova, N.A.; Kokorin, A.I.; Sviridov, D.V. Photoaccumulating TiO_2–MoO_3, TiO_2–V_2O_5, and TiO_2–WO_3 Heterostructures for Self-Sterilizing Systems with the Prolonged Bactericidal Activity. *Catal. Lett.* **2019**, *149*, 1147–1153. [CrossRef]
22. Shahmoradi, Y.; Souri, D.; Khorshidi, M. Glass-ceramic nanoparticles in the Ag_2O–TeO_2–V_2O_5 system: Antibacterial and bactericidal potential, their structural and extended XRD analysis by using Williamson–Smallman approach. *Ceram. Int.* **2019**, *45*, 6459–6466. [CrossRef]
23. Karasenkov, Y.; Frolov, G.; Pogorelsky, I.; Latuta, N.; Gusev, A.; Kuznetsov, D.; Leont'ev, V. Colloidal metal oxide nanoparticle systems: The new promising way to prevent antibiotic resistance during treatment of local infectious processes. In Proceedings of the 3rd International Youth Conference on Interdisciplinary Problems of Nanotechnology, Biomedicine and Nanotoxicology (Nanobiotech), Tambov, Russia, 21–22 May 2015.
24. Li, P.; Feng, Y.; Cheng, D.; Wei, J. Self-template synthesis of mesoporous vanadium oxide nanospheres with intrinsic peroxidase-like activity and high antibacterial performance. *J. Colloid Interface Sci.* **2022**, *625*, 435–445. [CrossRef] [PubMed]
25. Li, J.; Liu, W.; Zhang, X.; Chu, P.K.; Cheung, K.M.C.; Yeung, K.W.K. Temperature-responsive tungsten doped vanadium dioxide thin film starves bacteria to death. *Mater. Today* **2019**, *22*, 35–49. [CrossRef]
26. Li, J.; Zhou, H.; Wang, J.; Wang, D.; Shen, R.; Zhang, X.; Jin, P.; Liu, X. Oxidative stress-mediated selective antimicrobial ability of nano-VO2 against Gram-positive bacteria for environmental and biomedical applications. *Nanoscale* **2016**, *8*, 11907–11923. [CrossRef] [PubMed]
27. Raj, S.; Kumar, S.; Chatterjee, K. Facile synthesis of vanadia nanoparticles and assessment of antibacterial activity and cytotoxicity. *Mater. Technol.* **2016**, *31*, 562–573. [CrossRef]
28. Prasanna, L.V.; Vijayaraghavan, R. Chemical manipulation of oxygen vacancy and antibacterial activity in ZnO. *Mater. Sci. Eng. C-Mater. Biol. Appl.* **2017**, *77*, 1027–1034.
29. Krishnamoorthy, K.; Manivannan, G.; Kim, S.J.; Jeyasubramanian, K.; Premanathan, M. Antibacterial activity of MgO nanoparticles based on lipid peroxidation by oxygen vacancy. *J. Nanopart. Res.* **2012**, *14*, 1063. [CrossRef]
30. Chen, C.; Wang, Y.; Zhang, D. Oxygen vacancy tuned oxidase mimic through selenium-doping ultrathin 2D Ni-V mixed metal oxide and antibacterial application. *J. Alloys Compd.* **2022**, *915*, 165446. [CrossRef]
31. Zhang, S.; Zou, Z.; Zhang, H.; Liu, J.; Zhong, S. Al/Ga co-doped V_6O_{13} nanorods with high discharge specific capacity as cathode materials for lithium-ion batteries. *J. Electroanal. Chem.* **2021**, *890*, 115220. [CrossRef]

32. Yang, H.; Ning, P.; Zhu, Z.; Yuan, L.; Jia, W.; Wen, J.; Xu, G.; Li, Y.; Cao, H. Water-steam activation toward oxygen-deficient vanadium oxides for enhancing zinc ion storage. *J. Mater. Chem. A* **2021**, *9*, 24517–24527. [CrossRef]
33. Fan, L.L.; Chen, S.; Wu, Y.F.; Chen, F.H.; Chu, W.S.; Chen, X.; Zou, C.W.; Wu, Z.Y. Growth and phase transition characteristics of pure M-phase VO2 epitaxial film prepared by oxide molecular beam epitaxy. *Appl. Phys. Lett.* **2013**, *103*, 131914. [CrossRef]
34. Kajita, S.; Eda, T.; Feng, S.; Tanaka, H.; Bieberle-Hutter, A.; Ohno, N. Increased Photoelectrochemical Performance of Vanadium Oxide Thin Film by Helium Plasma Treatment with Auxiliary Molybdenum Deposition. *Adv. Energy Sustain. Res.* **2023**, *4*, 2200141. [CrossRef]
35. Meng, J.; Zhang, S.; Liu, X.; Zhong, S.; Zou, Z. Facile synthesis of 3D urchin-like V_6O_{13} microflowers as cathode materials for high-capacity and high-rate lithium-ion batteries. *J. Electroanal. Chem.* **2021**, *900*, 115742. [CrossRef]
36. Horiuchi, S.; Saeki, M.; Matsui, Y.; Nagata, F. Transition of V_6O_{13} to VO_2 observed with a high-resolution electron microscope. *Acta Crystallogr. Sect. A* **1975**, *31*, 660–664. [CrossRef]
37. Gao, S.; Chen, Y.; Luo, H.; Jiang, L.; Ye, B.; Wei, M.; Wei, K. Single-Crystal Vanadium Pentoxide Nanowires. *J. Nanosci. Nanotechnol.* **2008**, *8*, 3500–3503. [CrossRef] [PubMed]
38. Hu, J.; Chen, H.; Xiang, K.; Xiao, L.; Chen, W.; Liao, H.; Chen, H. Preparation for V_6O_{13}@hollow carbon microspheres and their remarkable electrochemical performance for aqueous zinc-ion batteries. *J. Alloys Compd.* **2021**, *856*, 157085. [CrossRef]
39. Lv, T.-T.; Zou, Z.-G.; Li, Y.-W.; Zhang, S.-C. Flower-like $Li_{0.36}V_6O_{13}$ with superior cycling stability as a cathode material for lithium-ion batteries. *Ionics* **2020**, *26*, 1181–1187. [CrossRef]
40. Zeng, H.M.; Zhao, Y.; Hao, Y.J.; Lai, Q.Y.; Huang, J.H.; Ji, X.Y. Preparation and capacitive properties of sheet V_6O_{13} for electrochemical supercapacitor. *J. Alloys Compd.* **2009**, *477*, 800–804. [CrossRef]
41. Li, S.; Zou, Z.; Wu, X.; Zhang, Y. Solvothermal preparation of carbon coated V_6O_{13} nanocomposite as cathode material for lithium-ion battery. *J. Electroanal. Chem.* **2019**, *846*, 113173. [CrossRef]
42. Mydeen, S.S.; Kumar, R.R.; Kottaisamy, M.; Vasantha, V.S. Biosynthesis of ZnO nanoparticles through extract from Prosopis juliflora plant leaf: Antibacterial activities and a new approach by rust-induced photocatalysis. *J. Saudi Chem. Soc.* **2020**, *24*, 393–406. [CrossRef]
43. Chen, L.Q.M.W.; Peng, J.F.; Xu, Q.; Zhu, Q.Y. FTIR study of vanadium oxide nanotubes from lamellar structure. *J. Mater. Sci.* **2004**, *39*, 2625–2627. [CrossRef]
44. Gupta, K.; Kumar, S.; Singhal, R. Effect of annealing and swift heavy ions irradiation on vanadium oxide thin films. *Radiat. Eff. Defects Solids* **2021**, *176*, 673–680. [CrossRef]
45. Debata, S.; Sharma, P.K. Design of CdV_2O_4-V_6O_{13} micro flowers for non-enzymatic electrochemical detection of urea. In Proceedings of the DAE Solid State Physics Symposium 2018, Hisar, India, 18–22 December 2018.
46. Akande, A.A.; Linganiso, E.C.; Dhonge, B.P.; Rammutla, K.E.; Machatine, A.; Prinsloo, L.; Kunert, H.; Mwakikunga, B.W. Phase evolution of vanadium oxides obtained through temperature programmed calcinations of ammonium vanadate in hydrogen atmosphere and their humidity sensing properties. *Mater. Chem. Phys.* **2015**, *151*, 206–214. [CrossRef]